electronics

Article

Improving Steady State Accuracy in Field-Weakened Six-Phase Induction Machines with Integrator and Modulated Predictive Control

Magno Ayala [1,*], Jesus Doval-Gandoy [2,*], Jorge Rodas [1], Osvaldo Gonzalez [1], Raúl Gregor [1], Larizza Delorme [1], Carlos Romero [1] and Ariel Fleitas [1]

[1] Laboratory of Power and Control Systems (LSPyC), Facultad de Ingeniería, Universidad Nacional de Asunción, Luque 2060, Paraguay; jrodas@ing.una.py (J.R.); ogonzalez@ing.una.py (O.G.); rgregor@ing.una.py (R.G.); ldelorme@ing.una.py (L.D.); cromero@ing.una.py (C.R.); afleitas@fiuna.edu.py (A.F.)
[2] Applied Power Electronics Technology (APET) Research Group, University of Vigo, 36310 Vigo, Spain
* Correspondence: mayala@ing.una.py (M.A.); jdoval@uvigo.es (J.D.-G.)

Abstract: Finite-control-set model predictive control techniques are considered an exciting option for high-performance control multiphase drives due to their fast dynamic response, ability to handle multiple targets and constraints, and adaptability to different power converters or machine models. However, these techniques have some drawbacks, such as poor current reduction ($x - y$) and steady-state error ($d - q$), especially in the field weakening zone. Although some proposals have addressed these issues by adding modulation stages or designing new cost functions, there is still room for improvement, especially in steady-state error reduction. Therefore, this article proposes to include an integrator attached to a modulated predictive current controller applied to a six-phase induction machine to improve its performance throughout the entire speed range regarding steady-state error mitigation. Experimental tests were carried out to validate the effectiveness of the proposed controller. Tests were carried out evaluating the reduction of the steady-state error ($d - q$), the current tracking, the ($x - y$) currents reduction and the total harmonic distortion.

Keywords: field weakening operation; multiphase induction machine; predictive current control; space vector modulation; steady-state error

Citation: Ayala, M.; Doval-Gandoy, J.; Rodas, J.; Gonzalez, O.; Gregor, R.; Delorme, L.; Romero, C.; Fleitas, A. Improving Steady State Accuracy in Field-Weakened Six-Phase Induction Machines with Integrator and Modulated Predictive Control. *Electronics* **2024**, *13*, 952. https://doi.org/10.3390/electronics13050952

Academic Editor: Jianguo Zhu

Received: 29 January 2024
Revised: 27 February 2024
Accepted: 28 February 2024
Published: 1 March 2024

1. Introduction

The scientific and industrial communities have shown significant interest in multiphase machines due to their remarkable characteristics, including but not limited to lower current per phase, intrinsic fault tolerance, lower torque ripple and superior harmonic filtering, compared to their three-phase equivalent [1,2]. Applied cntrollers for this type of machine are generally based on techniques developed for three-phase versions, such as field-oriented control (FOC) based on internal proportional-integral (PI) current control or direct torque control [3–5].

Recently, there have been advances in nonlinear control algorithms for multiphase machines [6]. Among them, the finite control version of model predictive control (FCS-MPC) has become the most studied for its intuitive nature, ease of implementation in digital systems, and fast response speed compared to other developed controllers [7–9]. FCS-MPC offers certain advantages, such as handling multiple targets and constraints, adapting to different power converters or machine models, and controlling linear and non-linear systems. Other types of FCS-MPC have been developed to address their limitations, such as ($x - y$) current reduction and computational burden reduction [10–13]. In the realm of FCS-MPC, an eye-catching limitation is the steady-state error. As a result, various solutions have been proposed to solve this undesirable behaviour, specifically in the context of

FCS-MPC applied to different power converters with RL load [14,15], permanent magnet synchronous machines [16,17] and induction machines [18]. Considering those applied to induction machines, limitations can be observed in their transient response analysis; and particularly, its performance in areas of field weakening was not verified. This article differs from others in that it proposes the elimination of steady-state error in an asymmetrical six-phase induction machine (ASPIM), especially in the field weakening zone, where the error is more noticeable [19,20]. To achieve this, it is proposed to utilize different simple, straightforward controllers in conjunction with the modulated predictive current control (MPCC) proposed in [21]. MPCC successfully addresses other limitations of FCS-MPC and extends its capabilities to high-speed conditions, including field weakening (FW) operations. This article differs from previous ones in that simple algorithms will be proposed to correct the steady-state error, including in the FW zone, and several techniques based on integrators will be compared to obtain a complete analysis in both steady and transient regimes.

Then, this article proposes the implementation of an MPCC with simple, straightforward controllers based on integrator variants to eliminate steady-state error, applied to an ASPIM in the entire speed range, including FW operations. The evaluation of the controller is demonstrated through experimental results, which optimizes the application of MPCC to multiphase machines. The results will be discussed regarding the steady-state error of $(d-q)$ currents, $(\alpha-\beta)$ currents tracking, $(x-y)$ currents reduction by considering the mean square error (MSE), mean value error (MVE) and the total harmonic distortion (THD) of stator currents as figures of merit.

The rest of this document is organized as follows: The ASPIM mathematical model is shown in Section 2. Section 3 presents the proposed controller, including the FCS-MPC design, as a predictive current control (PCC). Section 3 also describes the design of the MPCC, including an FW algorithm. The experimental results show the steady-state and transient behaviour for the proposed technique, where the figures of merit are discussed in Section 4. Finally, the conclusions are summarized in Section 5.

2. ASPIM Model Description

The FCS-MPC strategy makes use of the mathematical model of the system, which is composed of an ASPIM fed through a six-leg voltage source inverter (VSI) connected to a DC voltage source as shown in Figure 1. In this respect, a continuous mathematical model of the ASPIM can be defined by differential equations. To simplify the six-dimensional space of the model with six phases (a, b, c, d, e, f), the vector space decomposition (VSD) technique was considered, that allows the analysis to be performed through three two-dimensional orthogonal planes in the stationary frame references denoted as $(\alpha-\beta)$, $(x-y)$ and (z_1-z_2), using (1) and based on the invariant amplitude criterion [22]. In addition, the ASPIM has a phase shift of 30° between the three-phase systems along with an isolated neutral configuration; therefore, it is assumed that the currents (z_1-z_2) are zero. The adoption of the VSD approach imparts a significant physical significance to the current profiles. Specifically, the alfa-beta current components are associated with electromechanical energy conversion. In contrast, the $(x-y)$ components primarily contribute to the machine's losses and do not actively participate in torque and flux generation. This clear distinction between the two sets of current components enhances the understanding and interpretation of the machine's operation and facilitates the implementation of FCS-MPC for improved performance.

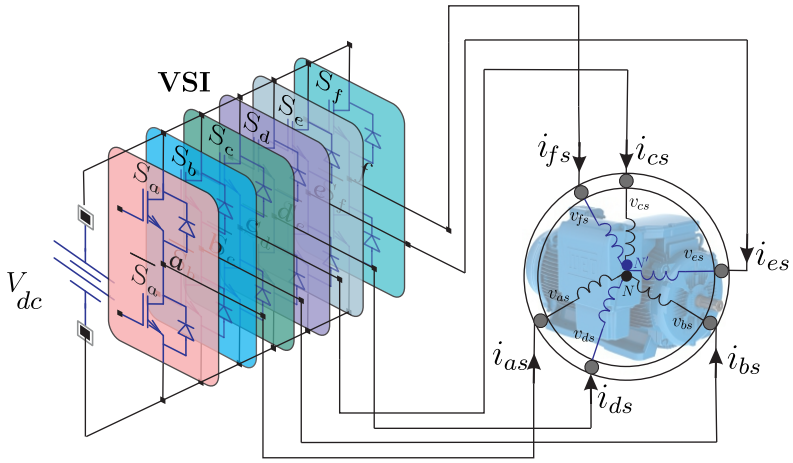

Figure 1. Scheme of ASPIM powered by a six-leg VSI.

$$\mathbf{T} = \frac{1}{3}\begin{bmatrix} 1 & \frac{\sqrt{3}}{2} & -\frac{1}{2} & -\frac{\sqrt{3}}{2} & -\frac{1}{2} & 0 \\ 0 & \frac{1}{2} & \frac{\sqrt{3}}{2} & \frac{1}{2} & -\frac{\sqrt{3}}{2} & -1 \\ 1 & -\frac{\sqrt{3}}{2} & -\frac{1}{2} & \frac{\sqrt{3}}{2} & -\frac{1}{2} & 0 \\ 0 & \frac{1}{2} & -\frac{\sqrt{3}}{2} & \frac{1}{2} & \frac{\sqrt{3}}{2} & -1 \\ 1 & 0 & 1 & 0 & 1 & 0 \\ 0 & 1 & 0 & 1 & 0 & 1 \end{bmatrix} \begin{matrix} \alpha \\ \beta \\ x \\ y \\ z_1 \\ z_2 \end{matrix} \quad \begin{matrix} a & d & b & e & c & f \end{matrix} \tag{1}$$

On the other hand, the six-phase VSI consists of two isolated gate bipolar transistors (IGBT) per phase. This VSI has discrete behaviour with a total number of $2^6 = 64$ possible switching outputs defined by six-legs. The combination of the different switching states and the DC voltage source sets the voltages per phase. The 64 possibilities of the voltages, according to the VSD approach, are represented in Figure 2 in which only 49 different vectors (48 vectors + 1 null vector) are considered different in $(\alpha - \beta)$ and $(x - y)$ planes. Hence, the state-space mathematical model of ASPIM can be written as follows:

$$\dot{\mathbf{X}}_{(t)} = \mathbf{A}_{(t)}\,\mathbf{X}_{(t)} + \mathbf{B}_{(t)}\,\mathbf{U}_{(t)} + \mathbf{H}\,\varpi_{(t)} \tag{2}$$

where $\mathbf{X}_{(t)} = [x_1, x_2, x_3, x_4, x_5, x_6]^T$ is the state vector that represents the stator and rotor currents $x_1 = i_{\alpha s}$, $x_2 = i_{\beta s}$, $x_3 = i_{xs}$, $x_4 = i_{ys}$, $x_5 = i_{\alpha r}$ and $x_6 = i_{\beta r}$, $\mathbf{U}_{(t)} = [u_1, u_2, u_3, u_4]^T = \left[v_{\alpha s}, v_{\beta s}, v_{xs}, v_{ys}\right]^T$ is the input vector applied to the stator coils, $\mathbf{H}$ is considered the noise weight matrix, the process noise is defined as $\varpi_{(t)}$ and $\mathbf{A}_{(t)}$ and $\mathbf{B}_{(t)}$ are matrices including the physical parameters of the ASPIM as follows:

$$\mathbf{A}_{(t)} = \begin{bmatrix} -R_s c_2 & c_4 L_m \omega_r & 0 & 0 & c_4 R_r & c_4 L_r \omega_r \\ c_4 L_m \omega_r & -R_s c_2 & 0 & 0 & c_4 L_r \omega_r & c_4 R_r \\ 0 & 0 & -R_s c_3 & 0 & 0 & 0 \\ 0 & 0 & 0 & -R_s c_3 & 0 & 0 \\ R_s c_4 & -c_5 L_m \omega_r & 0 & 0 & -c_5 R_r & -c_5 L_r \\ -c_5 L_m \omega_r & R_s c_4 & 0 & 0 & -c_5 L_r & -c_5 R_r \end{bmatrix}$$

$$\mathbf{B}_{(t)} = \begin{bmatrix} c_2 & 0 & 0 & 0 \\ 0 & c_2 & 0 & 0 \\ 0 & 0 & c_3 & 0 \\ 0 & 0 & 0 & c_3 \\ -c_4 & 0 & 0 & 0 \\ 0 & -c_4 & 0 & 0 \end{bmatrix}$$

being R_s, R_r, L_m (mutual inductance), $L_r = L_{lr} + L_m$ and $L_s = L_{ls} + L_m$ the electrical parameters of the ASPIM. The coefficients are defined as $c_1 = L_s L_r - L_m^2$, $c_2 = \frac{L_r}{c_1}$, $c_3 = \frac{1}{L_{ls}}$, $c_4 = \frac{L_m}{c_1}$ and $c_5 = \frac{L_s}{c_1}$.

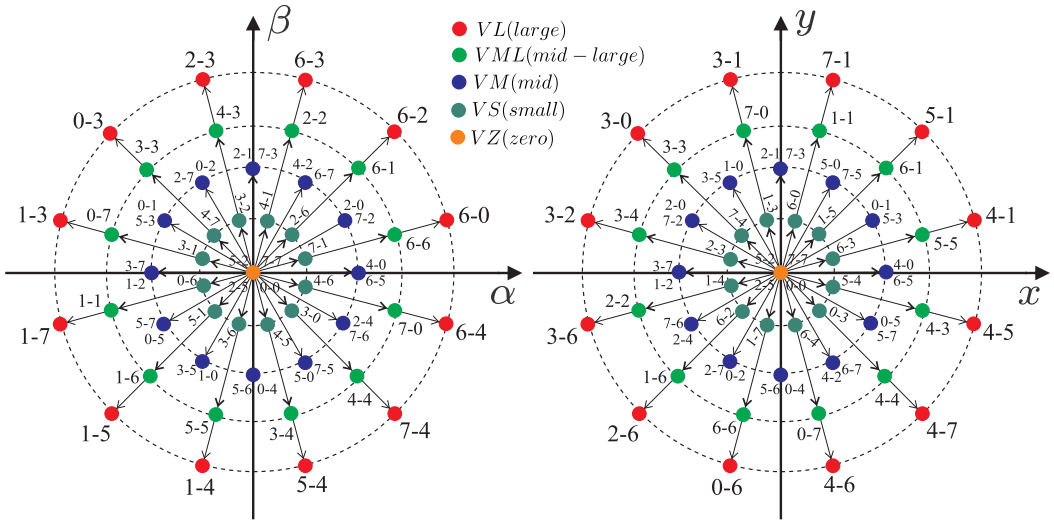

Figure 2. Voltage space vectors and 64 switching states in $(\alpha - \beta)$ and $(x - y)$ planes for an ASPIM.

The ideal VSI mathematical model has been selected to obtain a good optimization process. Stator voltages depend on the input control switching state denoted as **S**, where $\mathbf{S} = [S_a, S_d, S_b, S_e, S_c, S_f]$, $\mathbf{S}_i \in \{0, 1\}$ and can be calculated from the ideal six-leg VSI model $\mathbf{M}_{[\mathbf{S}]}$ as follows:

$$\mathbf{M}_{[\mathbf{S}]} = \frac{1}{3} \begin{bmatrix} 2 & 0 & -1 & 0 & -1 & 0 \\ 0 & 2 & 0 & -1 & 0 & -1 \\ -1 & 0 & 2 & 0 & -1 & 0 \\ 0 & -1 & 0 & 2 & 0 & -1 \\ -1 & 0 & -1 & 0 & 2 & 0 \\ 0 & -1 & 0 & -1 & 0 & 2 \end{bmatrix} \mathbf{S}^T. \tag{3}$$

The ideal six-leg VSI converts the switching signals into phase voltages, which are transformed to $(\alpha - \beta)$ and $(x - y)$ planes, and they are defined in $\mathbf{U}_{(t)}$ as follows:

$$\mathbf{U}_{(t)} = V_{DC}\, \mathbf{T}\, \mathbf{M}_{[\mathbf{S}]}. \tag{4}$$

where V_{DC} is the DC voltage source. The output vector, **Y**, is:

$$\mathbf{Y}_{(t)} = \mathbf{C}\, \mathbf{X}_{(t)} + \nu_{(t)} \tag{5}$$

where $\nu_{(t)}$ is considered the measurement noise and

$$\mathbf{C} = \begin{bmatrix} 1 & 0 & 0 & 0 & 0 & 0 \\ 0 & 1 & 0 & 0 & 0 & 0 \\ 0 & 0 & 1 & 0 & 0 & 0 \\ 0 & 0 & 0 & 1 & 0 & 0 \end{bmatrix}.$$

The torque of the ASPIM is obtained through the following equations:

$$T_e = 3\, P \left(\psi_{\alpha s} i_{\beta s} - \psi_{\beta s} i_{\alpha s} \right) \tag{6}$$

$$J_i\, \dot{\omega}_m + B_i\, \omega_m = (T_e - T_L) \tag{7}$$

$$\omega_r = P\omega_m \tag{8}$$

where T_e represents the electromagnetic torque, P the number of pole pairs, $\psi_{\alpha s}$ and $\psi_{\beta s}$ are the stator fluxes, J_i is the inertia coefficient, B_i the friction coefficient, T_L is the load torque, ω_r is the rotor electrical angular speed, and ω_m the rotor mechanical speed.

3. Proposed Control Applied to the ASPIM

This section also presents the complete control structure consisting of outer speed control, an inner PCC including a reduced order observer, the cost function design, the modulation stage, the high-speed operation with FW and a steady-state current regulator based on an integrator and a lead compensator.

3.1. Mechanical Speed Control

The ASPIM speed regulation is achieved by implementing a PI controller with saturator and an anti-windup algorithm, as proposed in [23]. This choice is based on its notable simplicity and robustness. The PI speed regulator is critical in generating the dynamic current reference, denoted as i_{qs}. Then, the slip frequency (ω_{sl}) estimation is carried out in an equivalent process as the indirect rotor field-oriented control (IRFOC) technique through the $d-q$ stator current references (i^*_{ds}, i^*_{qs}) and the rotor parameters R_r, L_r of the ASPIM. The following equation can define the speed control:

$$i^*_{qs} = K_p(\omega^*_m - \omega_m) + \frac{K_i(\omega^*_m - \omega_m)}{z-1} \tag{9}$$

3.2. PCC Based on FCS-MPC

The typical control scheme for the predictive current control based on FCS-MPC is shown in Figure 3. The primary aspect of predictive control involves utilizing a system model to anticipate the forthcoming actions of the controlled parameters. The values of the controlled variables, stator current, are acquired at each sampling instant (k) and are used to predict the output value for the next sampling instant $(k+1)$. These calculations, considering the system behavior, are represented by the block called the prediction module. First, the output is calculated for sampling instant $(k+1)$, then for $(k+2)$. The controller utilizes these calculations to achieve optimal performance based on the predefined optimization criterion referred to in this case as the cost function. In the case of classical predictive control, the objective is to minimize the error between the value of the measured control variable and the predicted value. However, the cost function can be adjusted for other control techniques to define different control criteria. This process is repeated for each sampling time considering the newly measured data.

To enable the PCC to function effectively, the state-space model of the ASPIM ((2) and (5)) needs to be transformed into a discrete form, and for this purpose, a direct Euler method is chosen to minimize computational complexity. The resulting equations will be in digital format, with predicted variables depending on past values rather than current ones. Therefore, the prediction of the following sample state, denoted as $\hat{\mathbf{X}}_{[k+1|k]}$, is defined as follows:

$$\hat{\mathbf{X}}_{[k+1|k]} = \mathbf{X}_{[k]} + \mathrm{f}\Big(\mathbf{X}_{[k]},\, \mathbf{U}_{[k]},\, T_s,\, \omega_{r[k]}\Big) \tag{10}$$

where $[k]$ is the current sample, f the function nomenclature and T_s is the sampling time.

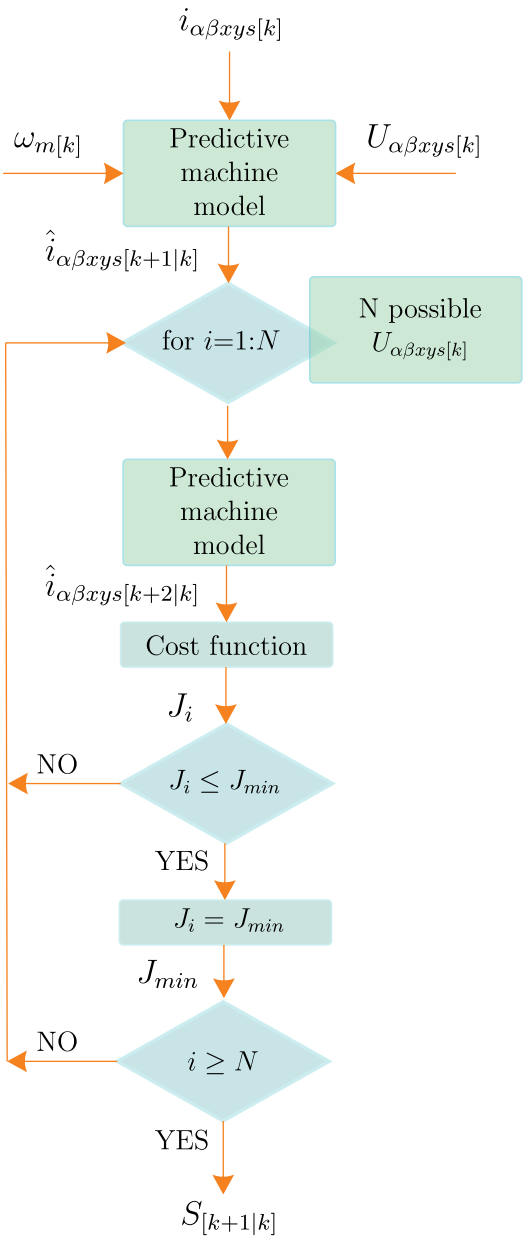

Figure 3. Flowchart for PCC based on FCS-MPC strategy.

3.3. Reduced Order Current Observers

In the state-space model (2), only the stator currents and the mechanical speed of the rotor are measured [24]. The stator voltages are calculated from the switching commands sent to the six-leg VSI. However, the rotor currents need to be observed. This is achieved through the concept of reduced-order observers. Low-order observers only estimate the value of the unmeasured parts of the state vector. This has been resolved by using the Luenberger Observer (LO) [25,26] and Kalman Filter (KF) [27] techniques, where the KF is considered a better selection because the observer gains are optimized taking into account the noise input to the sensors. A profound explanation of the dynamics and error convergence of the KF can be found in [27], and it was not included in this work for conciseness.

3.4. Cost Function

The cost function problem allows optimization of essential variables, such as minimizing the torque ripple of the machine and minimizing the harmonic content [28]. However,

the most critical variable in current control is the following error in the predicted stator currents in the $(\alpha - \beta)$ and $(x - y)$ planes. PCC analyzes the cost function for iterations of 49 states with the following:

$$J_{[k+2|k]} = \Bigg[(i^*_{\alpha s[k+2]} - \hat{i}_{\alpha s[k+2|k]})^2 + (i^*_{\beta s[k+2]} - \hat{i}_{\beta s[k+2|k]})^2 + \lambda_{xy} \Big((i^*_{xs[k+2]} - \hat{i}_{xs[k+2|k]})^2 + (i^*_{ys[k+2]} - \hat{i}_{ys[k+2|k]})^2 \Big) \Bigg]^{\frac{1}{2}} \tag{11}$$

Using (12), it is possible to compute a second step forward prediction of the stator currents $\hat{i}_{s[k+2|k]}$ for the dead time compensation [27]. The stator current references are represented by $i^*_{s[k+2]}$. Optimizing the weighting factor is a contemporary research topic, and some papers have addressed this subject [29,30]. Typically, in multiphase machines, λ_{xy} allows for prioritizing the stator currents in the $(\alpha - \beta)$ plane.

$$\hat{\mathbf{X}}_{[k+2|k]} = \mathbf{A}_{[k]}\mathbf{X}_{[k+1]} + \mathbf{B}_{[k]}\mathbf{U}_{[k+1]} + \mathbf{H}\omega_{[k]} \tag{12}$$

3.5. Modulated PCC (MPCC)

MPCC is a technique based on space vector modulation (SVM). In this case, MPCC uses four vectors, including two mid vectors (VM) and two large vectors (VL). The main goal of this modulation is to improve the performance of the stator current tracking by including the adjacent VM per sector to avoid the application of null vectors (VZ). VZ reduces the range of the vectors in combination with its corresponding duty cycle, reducing the controller's performance of tracking the desired stator currents in the $(\alpha - \beta)$ plane. This is because the VZ duty cycle increases when the $(x - y)$ currents are being reduced [21]. The duty cycles for the four active vectors, d_1, d_2, d_3 and d_4, are calculated by solving the following equations:

$$d_1 = \frac{\sigma}{J_1} \quad d_2 = \frac{\sigma}{J_2} \quad d_3 = \frac{\sigma}{J_3} \quad d_4 = \frac{\sigma}{J_4} \tag{13}$$

$$d_1 + d_2 + d_3 + d_4 = 1 \tag{14}$$

where J_1, J_2, J_3 and J_4 are the defined cost function (11) for all the vectors in the selected sector. It is possible to calculate the equation for σ and the duty cycles for each vector given as follows:

$$d_1 = \frac{J_2 J_3 J_4}{J_1 J_3 J_4 + J_2 J_3 J_4 + J_1 J_2 J_4 + J_1 J_2 J_3} \tag{15}$$

$$d_2 = \frac{J_1 J_3 J_4}{J_1 J_3 J_4 + J_2 J_3 J_4 + J_1 J_2 J_4 + J_1 J_2 J_3} \tag{16}$$

$$d_3 = \frac{J_1 J_2 J_4}{J_1 J_3 J_4 + J_2 J_3 J_4 + J_1 J_2 J_4 + J_1 J_2 J_3} \tag{17}$$

$$d_4 = \frac{J_1 J_2 J_3}{J_1 J_3 J_4 + J_2 J_3 J_4 + J_1 J_2 J_4 + J_1 J_2 J_3} \tag{18}$$

MPCC evaluates 12 sectors, as shown in Figure 4, by calculating the cost function for each vector (48 in total), and then the duty cycles of each vector are calculated. Finally, the final cost function is computed as follows:

$$G_{[k+2|k]} = d_1 J_1 + d_2 J_2 + d_3 J_3 + d_4 J_4 \tag{19}$$

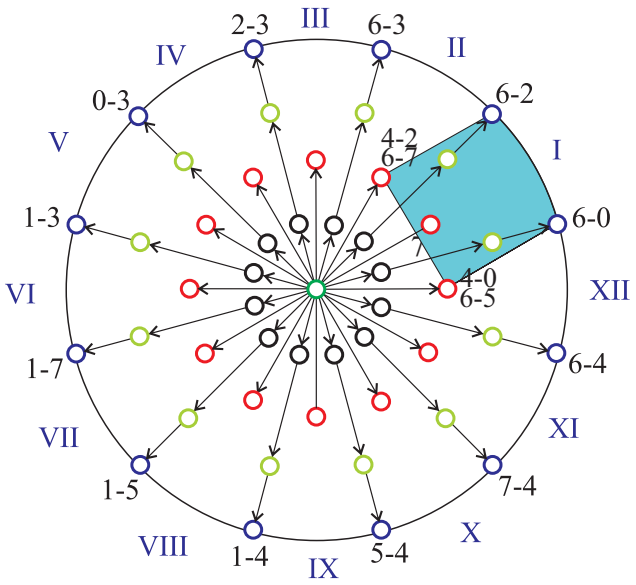

Figure 4. Active sectors of MPCC for the six-leg VSI.

3.6. Field Weakening Operation

For FW operations, the simplest method is to vary the rotor flux reference in inverse proportion to ω_m [31], weakening the magnetic field. In this method, above rated speed, the reference currents i^*_{ds} and i^*_{qs} are computed as follows:

$$i^*_{ds} = \frac{\omega_{m(rated)}}{\omega_m} i_{ds(rated)} \tag{20}$$

$$i^*_{qs(max)} = \sqrt{i^2_{s(max)} - i^{*2}_{ds}} \tag{21}$$

where $i_{s(max)}$ is the maximum possible stator current, normally set to 1.5 times the rated current [32]. Likewise, $i^*_{qs(max)}$ is the maximum possible reference in the case where there is no external speed control. Thus, in this proposal, it can be used to limit the output of the speed controller and limit i_{qs}, since this value is obtained from the speed control. Usually, when i^*_{ds} is decreased, to use the maximum current, i^*_{qs} can be increased as i^*_{ds} decreases.

3.7. Steady-State Current Regulator

MPCC effectively addresses numerous limitations of FCS-MPC, including the reduction of $(x - y)$ currents, low THD despite variable and low switching frequency, and smooth operation across all mechanical speeds up to the rated value even at low sampling frequency compared to the PCC without modulation [28]. However, it has one limitation: it fails to eliminate the steady-state error in $(d - q)$ currents despite optimal tracking in the $(\alpha - \beta)$ stator currents. This error worsens as speed increases and is amplified in FW operations.

For this reason, the inclusion of a steady-state error regulator for $(d - q)$ currents is proposed (MPCC-R), as shown in Figure 5.

The design criteria include a cascade integrator combined with the MPCC to eliminate the steady-state error in $(d - q)$ currents. This approach involves the following function [18]:

$$I(z) = \frac{K_R z^{-1}}{1 - z^{-1}} \tag{22}$$

Additionally, MPCC with a small sampling time is approximated to a closed-loop system with its eigenvalues at the origin of the complex plane, so it will be represented as a delay z^{-1} [18]. Although this representation is a limited version of a control like the MPC,

it is a simple way to analyze it, considering that an external control will be included. Then, the following closed-loop function is obtained:

$$\frac{i_{dqs}(z)}{i_{dqs}(z)^*} = \frac{K_R z^{-2}}{1 - z^{-1} + K_R z^{-2}} \tag{23}$$

where it can be verified that to stay on the unit circle, it must be satisfied that $0 < K_R < 1$. Finally, a saturator with anti-windup is included to provide greater security by limiting the $(d - q)$ currents.

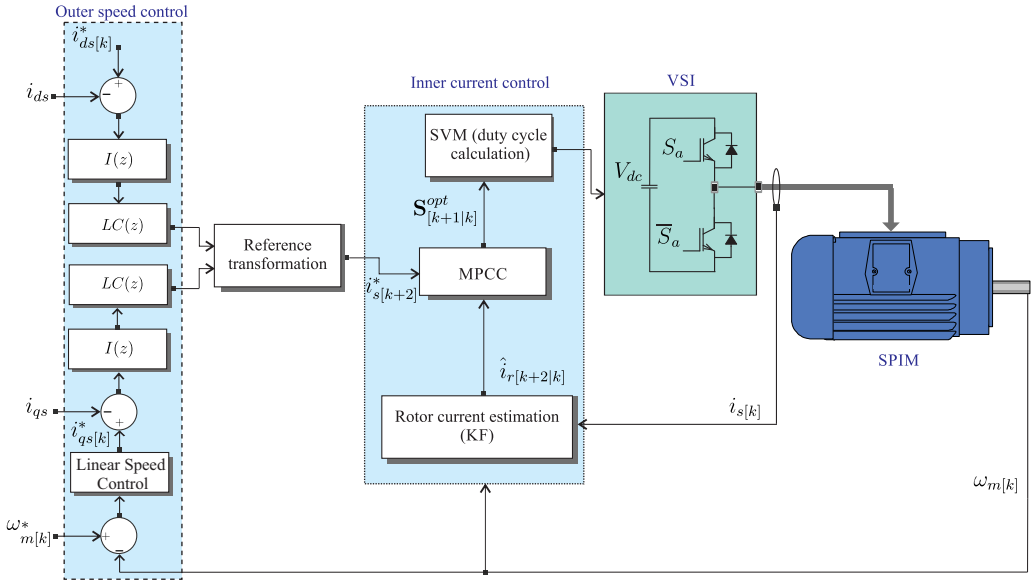

Figure 5. Block diagram of MPCC-R.

However, a simple integrator tends to have a slow response and presents oscillations in its dynamic behaviour, which the ASPIM could operate considering speed or load changes. For this reason, a lead compensator (LC) is included to speed up the dynamic response, since it is one of the controllers with the highest transient response speed and bandwidth. Typically, such a compensator is designed by some criteria regarding the position of the closed-loop poles or frequency domain behaviour. In this work, the selected criteria are due to the frequency domain behaviour of the simplified system shown in (23) to obtain 40° more of phase margin, improving the system bandwidth by amplifying the signal for frequencies higher than 6 Hz. The compensator has the following form:

$$LC(s) = \frac{Ts + 1}{\alpha Ts + 1} \tag{24}$$

where T is the compensator time, α the attenuation factor and s the Laplace operator. At the same time, its discrete equivalent with zero-order hold can be defined as follows:

$$LC(z) = \frac{\frac{z}{\alpha} + 1 - \frac{1}{\alpha} - e^{-\left(\frac{T_s}{\alpha T}\right)}}{z - e^{-\left(\frac{T_s}{\alpha T}\right)}} \tag{25}$$

As for the current regulator, parameters are selected as follows: $\alpha = 0.2$, $T = 0.24$, $K_R = 100T_s$.

For comparison purposes, a PI controller (named MPCC-PI) will be tested as an alternative for steady-state error elimination with the following tuning values: $K_{pr} = 1$ and $K_{ir} = 500$. These values are obtained by comparing the resulting gain of the compensator and integrator.

4. Experimental Results

An experimental test platform evaluates The proposed algorithm to verify its behaviour. This setup comprises an ASPIM, two conventional three-leg VSIs, and a DC power source. The VSIs are driven through a dSPACE MABXII DS1401 real-time rapid prototyping platform programmed with MATLAB/Simulink 2014a. The ASPIM parameters were estimated through stand-still tests and AC time domain conventional methods [33] and are presented in Table 1.

Table 1. Parameters of the ASPIM.

Parameter	Value	Parameter	Value
R_r (Ω)	6.9	R_s (Ω)	6.7
L_s (mH)	654.4	L_r (mH)	626.8
L_m (mH)	614	L_{ls} (mH)	5.3
ω_{m-nom} (rpm)	2 540	P_w (kW)	2
J_i (kg·m^2)	0.07	B_i (kg·m^2/s)	0.0004
P (pole pair)	1	$Slip$	0.1533
T_{e-nom} (Nm)	7.5	i_{s-rms} (A)	2.2

The currents were measured using LA 55-P s sensors, which have multiple turns to enhance accuracy at low measurements and a frequency range of DC up to 200 kHz. The measurements are then digitized using a 16-bit A/D converter. The mechanical angle of the ASPIM is obtained with a 1024 ppr incremental encoder, and the rotor speed is calculated from it. Moreover, a variable mechanical load is performed on the ASPIM using a 5 HP eddy current brake. Finally, a photo of the experimental setup is illustrated in Figure 6.

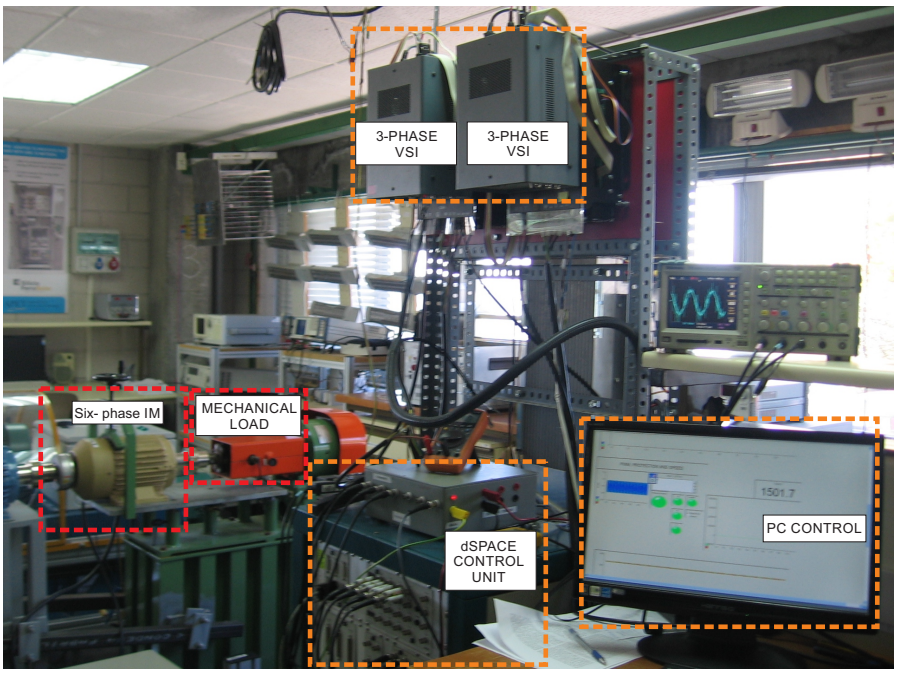

Figure 6. Photo of the experimental bench including the ASPIM, the dSPACE platform, the eddy current brake and the six-phase VSI.

The cost function in (11) with λ_{xy} = 0.1 was selected to evaluate the performance of the PCC [21]. The process and measurement noise values can be calculated using the autocovariance-least-squared (ALS) method since it provides unbiased estimates with the lowest covariance, guaranteeing optimal KF tuning [27]. The obtained values are $\hat{Q}_w = 0.0022$ and $\hat{R}_v = 0.0022$. Then, $(x-y)$ current references are set to zero ($i^*_{xs} = i^*_{ys} = 0$) since this plane is related only to the machine's losses and a fixed d current ($i^*_{ds} = 1$ A) has been considered in rated speed conditions. The sampling frequency is fixed at 16 kHz. Finally, the DC voltage is set to 600 V to perform nominal voltage conditions.

4.1. Figures of Merit

The analysis of the proposed technique in transient and steady-state conditions is evaluated by figures of merit such as MSE between the reference and measured stator currents in $(\alpha-\beta)$ and $(x-y)$ planes, MVE of $(d-q)$ currents and THD is also calculated in the $(\alpha-\beta)$ plane to complete the analysis. The MSE is defined as follows:

$$\text{MSE}(i_{s\Phi}) = \sqrt{\frac{1}{N}\sum_{k=1}^{N}(i_{s\Phi}[k] - i^*_{s\Phi}[k])^2} \tag{26}$$

where N is the number of analyzed samples, $i^*_{s\Phi}$ the stator current reference, $i_{s\Phi}$ the measured stator currents and $\Phi \in \{\alpha, \beta, x, y\}$. On the other hand, MVE is calculated as follows:

$$\text{MVE}(i_{s\theta}) = \left|\frac{100}{N}\sum_{k=1}^{N}(i_{s\theta}[k] - i^*_{s\theta}[k])\right| \tag{27}$$

where $i^*_{s\theta}$ is $(d-q)$ stator currents reference and $i_{s\theta}$ the measured currents. Finally, THD is defined as follows:

$$\text{THD}(i_s) = \sqrt{\frac{1}{i^2_{s1}}\sum_{j=2}^{N}(i_{sj})^2} \tag{28}$$

where i_{s1} is the fundamental stator currents and i_{sj} is the harmonic stator currents.

4.2. Steady-State Results

Steady-state tests are developed with different mechanical speeds: 500 rpm, 1000 rpm, 1500 rpm, 2000 rpm, 2550 rpm, (rated speed), 3000 rpm and 3400 rpm (FW conditions).

Table 2 shows the results for all the mechanical speeds for the MPCC without the steady-state current regulator, and in Table 3, the results are with the steady-state current regulator. Some of them are the MSE of the rotor speed and stator currents in $(\alpha-\beta)$ and $(x-y)$, MVE of the $(d-q)$ plane and THD for $(\alpha-\beta)$ stator currents.

The results show good performance from MPCC even at higher speeds regarding $(\alpha-\beta)$ and $(x-y)$ current tracking. However, the $(d-q)$ currents present high steady-state error for all speeds. The THD improves at higher rotor speeds because the high DC-link generates a higher voltage ripple. On the other hand, with the inclusion of the steady-state current regulator, almost all the figures of merit improve, especially the MVE for $(d-q)$ currents, which is practically zero in every case.

Table 2. Performance Behaviour of Stator Currents, MSE (A), MSE (rpm), MVE (%) and THD (%) for MPCC [21] at different mechanical speeds (rpm).

ω^*_m	MSE_α	MSE_β	MSE_x	MSE_y	MSE_{ω_m}
500	0.1546	0.1518	0.2655	0.2470	1.5650
1000	0.1602	0.1600	0.2638	0.2593	1.3316
1500	0.1687	0.1678	0.2911	0.2946	1.9202

Table 2. *Cont.*

ω_m^*	$\mathbf{MSE}_\alpha$	$\mathbf{MSE}_\beta$	$\mathbf{MSE}_x$	$\mathbf{MSE}_y$	$\mathbf{MSE}_{\omega_m}$
2000	0.1843	0.1890	0.3196	0.3219	2.0436
2550	0.2043	0.2156	0.3477	0.3507	3.1504
3000	0.2013	0.2037	0.3026	0.3094	3.2554
3400	0.2255	0.2334	0.3392	0.3471	3.8409
ω_m^*	$\mathbf{THD}_\alpha$	$\mathbf{THD}_\beta$	$\mathbf{MVE}_d$	$\mathbf{MVE}_q$	
500	20.87	21.18	2.77	6.57	
1000	19.79	19.29	3.36	8.16	
1500	15.65	16.20	3.17	8.55	
2000	13.75	14.22	0.22	9.09	
2550	12.21	12.63	2.68	9.33	
3000	16.50	17.54	0.60	12.75	
3400	13.81	14.61	6.44	11.26	

Table 3. Performance Behaviour of Stator Currents, MSE (A), MSE (rpm), MVE (%) and THD (%) for the proposed MPCC-R at different mechanical speeds (rpm).

ω_m^*	$\mathbf{MSE}_\alpha$	$\mathbf{MSE}_\beta$	$\mathbf{MSE}_x$	$\mathbf{MSE}_y$	$\mathbf{MSE}_{\omega_m}$
500	0.1545	0.1532	0.2693	0.2532	1.5877
1000	0.1536	0.1527	0.2764	0.2605	1.4949
1500	0.1548	0.1628	0.2894	0.2806	1.9880
2000	0.1611	0.1674	0.3053	0.3020	2.2003
2550	0.1610	0.1705	0.3308	0.3377	3.0439
3000	0.1596	0.1645	0.2872	0.2959	3.7133
3400	0.1781	0.1835	0.3210	0.3290	4.8528
ω_m^*	$\mathbf{THD}_\alpha$	$\mathbf{THD}_\beta$	$\mathbf{MVE}_d$	$\mathbf{MVE}_q$	
500	20.26	20.82	0.01	0.05	
1000	19.31	19.67	0.00	0.14	
1500	17.85	18.78	0.00	0.03	
2000	16.06	16.43	0.01	0.06	
2550	12.99	14.24	0.03	0.00	
3000	17.81	18.83	0.05	0.00	
3400	16.26	16.77	0.00	0.03	

Figure 7 presents the stator currents tracking in $(d-q)$ planes for MPCC and MPCC-R under different speed values. The tests were performed with a fixed eddy current to set a constant mechanical load. As for FW conditions, the brake is reduced. Thus, the amplitude of (q) varies slightly at different speeds.

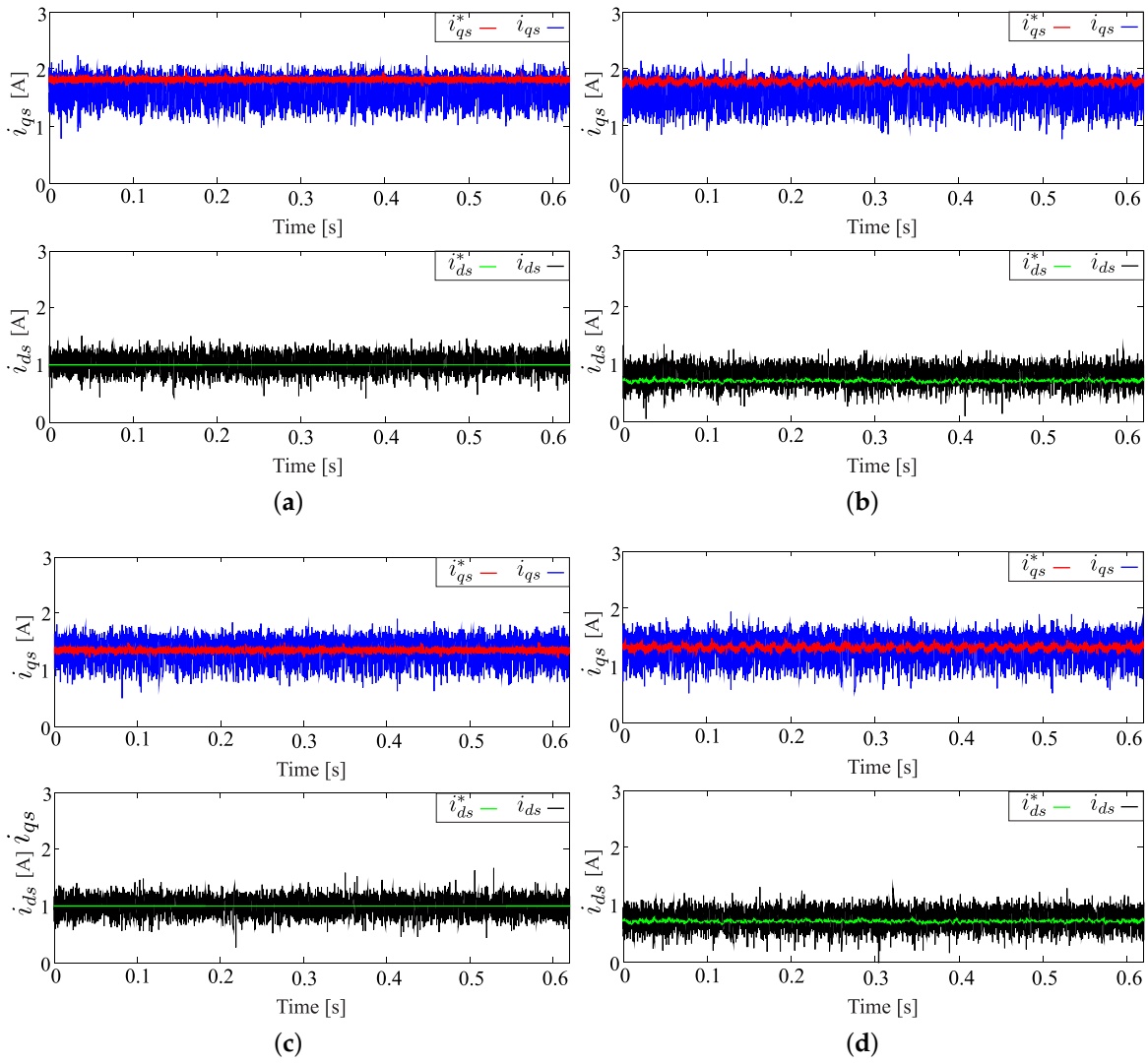

Figure 7. Stator currents i_{ds}, i_{ds}^* and i_{qs}, i_{qs}^* at different speeds for both MPCC and MPCC-R: (**a**) MPCC at 2550 rpm; (**b**) MPCC at 3400 rpm; (**c**) MPCC-R at 2550 rpm; (**d**) MPCC-R at 3400 rpm.

4.3. Transient Results

For the transient analysis, two steps in mechanical speed are considered, from 500 to −500 rpm (reversal condition) and from 500 to 2000 rpm (acceleration) for MPCC, MPCC-PI and MPCC-R. Figures 8 and 9 present the dynamic behaviour for MPCC, MPCC-PI and MPCC-R, which includes the current in the q axis and the currents in the $(\alpha - \beta)$ and $(x - y)$ planes. The step change (reversal) is shown at the instant of 5 ms where MPCC, MPCC-PI and MPCC-R reach at a time of 0.75, 6.5 and 4.5 ms for the q current, respectively. As for the acceleration test, the reaching time is 1 ms, 6 ms and 5.6 ms for MPCC, MPCC-PI and MPCC-R, respectively. There is no overshoot due to the selected gain of the integrator, which, if increased, would already present an overshoot. Thus, this value was adjusted to resemble the behaviour without an integrator; as shown, MPCC-R has a slower behaviour than MPCC and faster than MPCC-PI. The response could be faster by adjusting the gain, but it is fast enough for most applications.

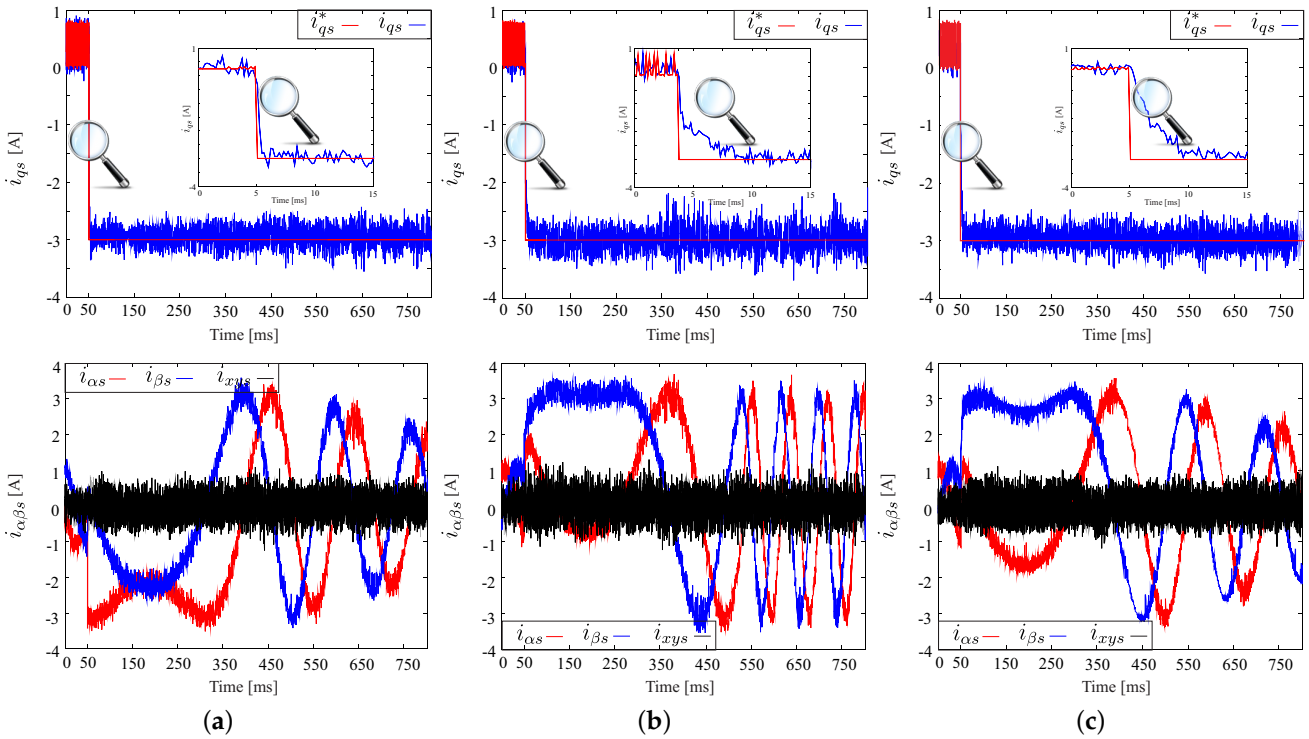

Figure 8. Transient response of stator currents (q), ($\alpha - \beta$) and ($x - y$) from a speed step response of 500 to −500 rpm (i_{qs} response of 0.5 to −3 A): (**a**) MPCC; (**b**) MPCC-PI; (**c**) MPCC-R.

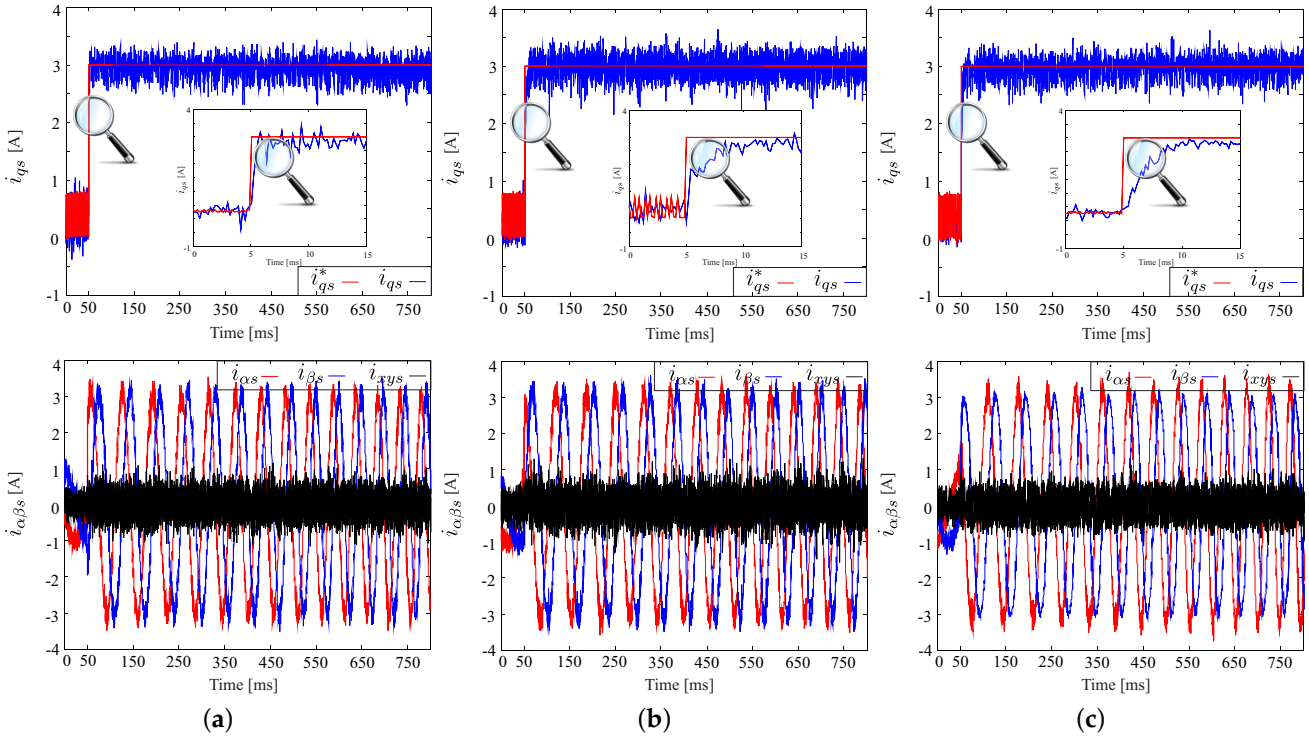

Figure 9. Transient response of stator currents (q), ($\alpha - \beta$) and ($x - y$) from a speed step response of 500 to 2000 rpm (i_{qs} response of 0.5 to 3 A): (**a**) MPCC; (**b**) MPCC-PI; (**c**) MPCC-R.

4.4. Discussion

Experimental results reveal that implementing the proposed control, coupled with adding integrators and lead compensators to MPCC, has led to noticeable enhancements in specific performance aspects of the ASPIM, as depicted in Figure 10. Regarding the MSE in the $(\alpha - \beta)$ and $(x - y)$ planes, an improvement has been observed, although not very significant. This suggests that the proposed technique has partially reduced the error in predicting the stator currents, especially at high operating speeds. On the other hand, in terms of THD, no apparent improvements are observed. The primary objective of this article is to achieve a significant reduction of the MVE in the $(d - q)$ plane; mainly, it was possible to eliminate this error in almost 100%, which is this paper's main contribution. The observed improvement in stator current tracking accuracy in this plane demonstrates the effectiveness of the proposed control approach. It is worth mentioning that the MSE improves since the steady-state error is almost eliminated, enhancing its performance, but the integrators have practically no effect in the $(\alpha - \beta)$ and $(x - y)$ planes where MPCC operates. Finally, the transient response has been slowed down by the inclusion of the integrators, but this can be accelerated again by increasing the gain of the same integrators; however, the system would present overshoots when the reference presents changes.

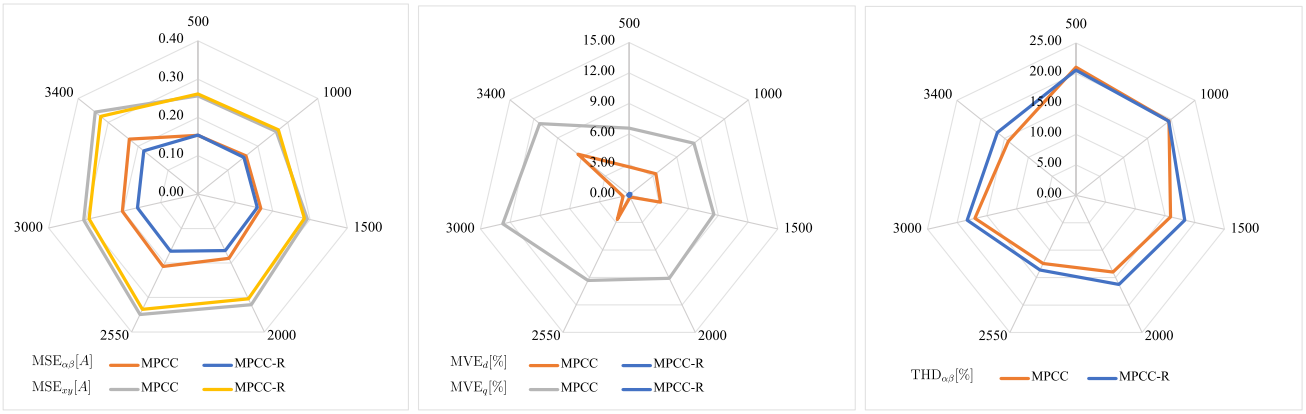

(**a**) (**b**) (**c**)

Figure 10. Performance behaviour of stator currents (**a**) MSE$\alpha\beta$ [A] and MSExy [A]; (**b**) MVEd [%] and MVEq [%]; (**c**) THD$\alpha\beta$ [%], from 500 [rpm] to 3400 [rpm] for MPCC and MPCC-R.

5. Conclusions

This article proposed the implementation of an MPCC with an integrator and a lead compensator to eliminate steady-state error, maintaining an excellent transient response, applied to an ASPIM in the entire speed range, including FW operations. The results show that the proposed control positively impacts stator current tracking. In the $(d - q)$ plane, there is an outstanding reduction in the MVE, which is less than 0.14% for all operating points, confirming the elimination of the steady-state error in almost 100%. As for MSE regarding stator currents tracking in the $(\alpha - \beta)$ and $(x - y)$ planes, there is a slight improvement compared to the MPCC without the external integrators, and the THD of $(\alpha - \beta)$ currents shows no change regarding the inclusion of the integrators. In addition, different control techniques based on integrators were compared to observe their performance in transient operations. The integrator with lead compensator named MPCC-R exhibited a higher response speed under conditions similar to MPCC without integrator. In summary, including the integrators completely corrects the steady-state error, significantly improving the controlled system.

Author Contributions: Conceptualization, M.A.; methodology, M.A. and J.D.-G.; software, M.A., J.D.-G. and O.G.; validation, J.D.-G. and M.A.; formal analysis, M.A., O.G., L.D. and C.R.; investigation, M.A., O.G., L.D., C.R. and A.F.; resources, J.D.-G. and M.A.; data curation, M.A. and O.G.; writing—original draft preparation, M.A., J.R., O.G., L.D., C.R. and R.G.; writing—review and editing, M.A., J.R., O.G., L.D., C.R., R.G. and A.F.; visualization, M.A. and J.D.-G.; supervision, M.A.; project administration, M.A. and O.G.; funding acquisition, M.A. All authors have read and agreed to the published version of the manuscript.

Funding: M. Ayala acknowledges the support of Conacyt through INIC01-35. J. Doval-Gandoy acknowledges the Government of Galicia under Grant GPC-ED431B 2023/12 and in part by the Spanish State Research Agency (AEI) under Project PID2022-136908OB-I00/MCIN/AEI/10.13039/501100011033/FEDER-UE.

Institutional Review Board Statement: Not applicable.

Informed Consent Statement: Not applicable.

Data Availability Statement: Data is contained within the article.

Acknowledgments: M. Ayala, J. Rodas, O. Gonzalez, R. Gregor, L. Delorme, and C. Romero acknowledge the support of the Consejo Nacional de Ciencia y Tecnología (CONACYT)-Paraguay through its PRONII program.

Conflicts of Interest: The authors declare no conflict of interest.

Abbreviations

The following abbreviations are used in this manuscript:

ASPIM	Asymmetrical six-phase induction machine
FCS-MPC	Finite control version of model predictive control
FOC	Field-oriented control
FW	Field weakening
IGBT	Isolated gate bipolar transistor
IRFOC	Indirect rotor field oriented control
KF	Kalman filter
LC	Lead compensator
LO	Luenberger observer
LV	Large vector
MV	Mid vector
MVE	Mean value error
MPCC	Modulated predictive control
MSE	Mean square error
PCC	Predictive current control
PI	Proportional-integral
SVM	Space vector modulation
THD	Total harmonic distortion
VSD	Vector space decomposition
VSI	Voltage source inverter
ZV	Null vector

References

1. Barrero, F.; Duran, M.J. Recent Advances in the Design, Modeling, and Control of Multiphase Machines: Part I. *IEEE Trans. Ind. Electron.* **2016**, *63*, 449–458. [CrossRef]
2. Duran, M.J.; Barrero, F. Recent Advances in the Design, Modeling, and Control of Multiphase Machines: Part II. *IEEE Trans. Ind. Electron.* **2016**, *63*, 459–468. [CrossRef]
3. Liu, Z.; Li, Y.; Zheng, Z. A review of drive techniques for multiphase machines. *CES Trans. Electr. Mach. Syst.* **2018**, *2*, 243–251. [CrossRef]
4. Prieto, I.G.; Duran, M.J.; Garcia-Entrambasaguas, P.; Bermudez, M. Field-oriented control of multiphase drives with passive fault tolerance. *IEEE Trans. Ind. Electron.* **2019**, *67*, 7228–7238. [CrossRef]
5. Muduli, U.R.; Behera, R.K.; Al Hosani, K.; El Moursi, M.S. Direct torque control with constant switching frequency for three-to-five phase direct matrix converter fed five-phase induction motor drive. *IEEE Trans. Power Electron.* **2022**, *37*, 11019–11033. [CrossRef]

6. Kali, Y.; Ayala, M.; Rodas, J.; Saad, M.; Doval-Gandoy, J.; Gregor, R.; Benjelloun, K. Current control of a six-phase induction machine drive based on discrete-time sliding mode with time delay estimation. *Energies* **2019**, *12*, 170. [CrossRef]
7. Rodriguez, J.; Kazmierkowski, M.P.; Espinoza, J.R.; Zanchetta, P.; Abu-Rub, H.; Young, H.; Rojas, C.A. State of the art of finite control set model predictive control in power electronics. *IEEE Trans. Ind. Inform.* **2013**, *9*, 1003–1016. [CrossRef]
8. Rodriguez, J.; Garcia, C.; Mora, A.; Flores-Bahamonde, F.; Acuna, P.; Novak, M.; Zhang, Y.; Tarisciotti, L.; Davari, S.A.; Zhang, Z.; et al. Latest advances of model predictive control in electrical drives—Part I: Basic concepts and advanced strategies. *IEEE Trans. Power Electron.* **2021**, *37*, 3927–3942. [CrossRef]
9. Mamdouh, M.; Abido, M.A. Simple Predictive Current Control of Asymmetrical Six-Phase Induction Motor with Improved Performance. *IEEE Trans. Ind. Electron.* **2022**, *70*, 7580–7590. [CrossRef]
10. Aciego, J.J.; Prieto, I.G.; Duran, M.J. Model predictive control of six-phase induction motor drives using two virtual voltage vectors. *IEEE J. Emerg. Sel. Top. Power Electron.* **2018**, *7*, 321–330. [CrossRef]
11. González-Prieto, I.; Durán, M.; Bermúdez, M.; Barrero, F.; Martín, C. Assessment of Virtual-Voltage-based Model Predictive Controllers in Six-phase Drives under Open-Phase Faults. *IEEE J. Emerg. Sel. Top. Power Electron.* **2019**, *8*, 2634–2644. [CrossRef]
12. Arahal, M.R.; Barrero, F.; Satué, M.G.; Ramírez, D.R. Predictive Control of Multi-Phase Motor for Constant Torque Applications. *Machines* **2022**, *10*, 211. [CrossRef]
13. Gonzalez, O.; Ayala, M.; Romero, C.; Delorme, L.; Rodas, J.; Gregor, R.; Gonzalez-Prieto, I.; Durán, M.J. Model predictive current control of six-phase induction motor drives using virtual vectors and space vector modulation. *IEEE Trans. Power Electron.* **2022**, *37*, 7617–7628. [CrossRef]
14. Lei, J.; Feng, S.; Wheeler, P.; Zhou, B.; Zhao, J. Steady-state error suppression and simplified implementation of direct source current control for matrix converter with model predictive control. *IEEE Trans. Power Electron.* **2019**, *35*, 3183–3194. [CrossRef]
15. Norambuena, M.; Lezana, P.; Rodriguez, J. A method to eliminate steady-state error of model predictive control in power electronics. *IEEE J. Emerg. Sel. Top. Power Electron.* **2019**, *7*, 2525–2530. [CrossRef]
16. Favato, A.; Carlet, P.G.; Toso, F.; Torchio, R.; Bolognani, S. Integral model predictive current control for synchronous motor drives. *IEEE Trans. Power Electron.* **2021**, *36*, 13293–13303. [CrossRef]
17. Goncalves, P.F.; Cruz, S.M.; Mendes, A.M. Disturbance observer based predictive current control of six-phase permanent magnet synchronous machines for the mitigation of steady-state errors and current harmonics. *IEEE Trans. Ind. Electron.* **2021**, *69*, 130–140. [CrossRef]
18. Wang, L.; Gan, L. Integral FCS predictive current control of induction motor drive. *IFAC Proc. Vol.* **2014**, *47*, 11956–11961. [CrossRef]
19. Jin, X.H.; Zhang, Y.; Xu, D.G. Static current error elimination algorithm for induction motor predictive current control. *IEEE Access* **2017**, *5*, 15250–15259. [CrossRef]
20. Oliani, I.; Figueiredo, R.; Lourenço, L.F.N.; Pelizari, A.; Sguarezi Filho, A.J. Robust Predictive Current Control Using Discrete-Time Integral Action for Induction Motors. *IEEE J. Emerg. Sel. Top. Power Electronics* **2023**, *11*, 5766–5773. [CrossRef]
21. Ayala, M.; Doval-Gandoy, J.; Rodas, J.; Gonzalez, O.; Gregor, R.; Rivera, M. A novel modulated model predictive control applied to six-phase induction motor drives. *IEEE Trans. Ind. Electron.* **2020**, *68*, 3672–3682. [CrossRef]
22. Zhao, Y.; Lipo, T. Space vector PWM control of dual three-phase induction machine using vector space decomposition. *IEEE Trans. Ind. Electron.* **1995**, *31*, 1100–1109. [CrossRef]
23. Harnefors, L.; Saarakkala, S.E.; Hinkkanen, M. Speed control of electrical drives using classical control methods. *IEEE Trans. Ind. Appl.* **2013**, *49*, 889–898. [CrossRef]
24. Satué, M.G.; Arahal, M.R.; Ortega, M.G.; Ramírez, D.R. A simple rotor current estimation method for predictive control of multi-phase drives. *Int. J. Circuit Theory Appl.* **2022**, *50*, 4478–4491. [CrossRef]
25. Martin, C.; Arahal, M.R.; Barrero, F.; Duran, M. Five-Phase Induction Motor Rotor Current Observer for Finite Control Set Model Predictive Control of Stator Current. *IEEE Trans. Ind. Electron.* **2016**, *63*, 4527–4538. [CrossRef]
26. Martin, C.; Arahal, M.R.; Barrero, F.; Duran, M. Multiphase rotor current observers for current predictive control: A five-phase case study. *Control Eng. Prac.* **2016**, *49*, 101–111. [CrossRef]
27. Rodas, J.; Barrero, F.; Arahal, M.R.; Martín, C.; Gregor, R. Online estimation of rotor variables in predictive current controllers: A case study using five-phase induction machines. *IEEE Trans. Ind. Electron.* **2016**, *63*, 5348–5356. [CrossRef]
28. Ayala, M.; Doval-Gandoy, J.; Gonzalez, O.; Rodas, J.; Gregor, R.; Rivera, M. Experimental stability study of modulated model predictive current controllers applied to six-phase induction motor drives. *IEEE Trans. Power Electron.* **2021**, *36*, 13275–13284. [CrossRef]
29. Novak, M.; Dragicevic, T.; Blaabjerg, F. Weighting factor design based on Artificial Neural Network for Finite Set MPC operated 3L-NPC converter. In Proceedings of the 2019 IEEE Applied Power Electronics Conference and Exposition (APEC), Anaheim, CA, USA, 17–21 March 2019; pp. 77–82. [CrossRef]
30. Majmunović, B.; Dragičević, T.; Blaabjerg, F. Multi Objective Modulated Model Predictive Control of Stand-Alone Voltage Source Converters. *IEEE J. Emerg. Sel. Top. Power Electron.* **2019**, *8*, 2559–2571. [CrossRef]
31. Xu, X.; Novotny, D.W. Selection of the flux reference for induction machine drives in the field weakening region. *IEEE Trans. Ind. Appl.* **1992**, *28*, 1353–1358. [CrossRef]

32. Kim, S.H.; Sul, S.K. Maximum torque control of an induction machine in the field weakening region. *IEEE Trans. Ind. Appl.* **1995**, *31*, 787–794. [CrossRef]
33. Riveros, J.A.; Yepes, A.G.; Barrero, F.; Doval-Gandoy, J.; Bogado, B.; Lopez, O.; Jones, M.; Levi, E. Parameter identification of multiphase induction machines with distributed windings Part 2: Time-domain techniques. *IEEE Trans. Energy Conv.* **2012**, *27*, 1067–1077. [CrossRef]